Master Thesis Report

June 23, 2014

Computer-Aided Comparative Assessment of Inflammatory Lesions in MRI of the Spine in Axial Spondyloarthritis Patients

Author:
Evgeni Aizenberg

Supervisors:
Dr. Oleh Dzyubachyk[2]
Prof. Boudewijn Lelieveldt[1,2]

Thesis committee members:
Dr. Emile Hendriks[1]
Dr. Anna Vilanova[1]
Dr. Rob J. van der Geest[2]
Dr. Oleh Dzyubachyk[2]

[1]Faculty of Electrical Engineering, Mathematics, and Computer Science
Delft University of Technology

[2]Division of Image Processing (LKEB)
Department of Radiology
Leiden University Medical Center

Thesis abstract

Detection of inflammatory lesions in magnetic resonance imaging (MRI) of the spine in axial Spondyloarthritis (SpA) patients is a labor-intensive task. Current scoring methods often require an expert reader to visually assess 23 vertebral units (VU) on multiple MRI slices. Furthermore, monitoring of progressive changes consists of a manual search and alignment of the 23 VUs in both baseline and follow-up scans, followed by side-by-side comparison of two images.

We present a semi-automated framework for comparative visualization of inflammatory lesions in MRI of the spine in axial SpA patients. The first part of our method localizes and segments the VUs using a fully automatic algorithm based on quasi-periodicity of vertebral column intensity profile and tissue class probability maps. The second part uses these segmentations to align baseline and follow-up scans by deriving a locally rigid transform from a pre-computed deformable registration. To facilitate visual comparison, the co-registered baseline and follow-up images are fused in a single color-encoded difference image. This allows an expert reader to efficiently interpret progressive changes while focusing on just one image.

Experiments in which an expert reader used the proposed framework to score inflammatory changes in axial SpA patients were performed. Results showed strong agreement with ground truth scores for cases of full lesion occurrence/remission.

Foreword

This thesis was carried out at the Division of Image Processing (LKEB) at the Radiology Department of Leiden University Medical Center (LUMC). The project was performed in the partial fulfillment of graduation requirements for the MSc degree in Electrical Engineering at Delft University of Technology (TU Delft).

Based on the completed work, it was decided to publish the developed methods and experimental results in the form of a scientific journal publication. The remainder of this thesis report consists of a self-contained journal article that is currently being prepared for submission to the *IEEE Transactions on Medical Imaging: special issue on Spine Imaging*. The journal article provides a comprehensive overview of related literature, the technical details of the proposed methods and their implementation, and the experimental results obtained in this thesis project.

Acknowledgements

I would like to express my sincere gratitude to my supervisors, Dr. Oleh Dzyubachyk and Prof. Boudewijn Lelieveldt, for their continuous guidance throughout all stages of my work and providing me with the opportunity to pursue a thesis project in the field of medical image processing at Leiden University Medical Center.

My special thanks goes to Rosaline van den Berg and Freek de Bruin for the numerous discussions and meetings we held that were essential for the development of this thesis. I would like to thank Manouk de Hooge, Pauline Bakker, Prof. Désirée van der Heijde, and Dr. Monique Reijnierse for their close collaboration throughout the project. Special thanks to Dr. Monique Reijnierse for the original idea of pursuing a thesis topic on computer-aided analysis of axial spondyloarthritis lesions.

Finally, I am sincerely thankful to my colleagues Denis Shamonin, Dr. Marius Staring, Baldur van Lew, and Dr. Ronald van ‘t Klooster for their time and help during my work on this project.

Computer-Aided Comparative Assessment of Inflammatory Lesions in MRI of the Spine in Axial Spondyloarthritis Patients

***Abstract*—Detection of inflammatory lesions in magnetic resonance imaging (MRI) of the spine in axial Spondyloarthritis (SpA) patients is a labor-intensive task. Current scoring methods often require an expert reader to visually assess 23 vertebral units (VU) on multiple MRI slices. Furthermore, monitoring of progressive changes consists of a manual search and alignment of the 23 VUs in both baseline and follow-up scans, followed by side-by-side comparison of two images. We present a semi-automated framework for comparative visualization of inflammatory lesions in MRI of the spine in axial SpA patients. The first part of our method localizes and segments the VUs using a fully automatic algorithm based on quasi-periodicity of vertebral column intensity profile and tissue class probability maps. The second part uses these segmentations to align baseline and follow-up scans by deriving a locally rigid transform from a pre-computed deformable registration. To facilitate visual comparison, the co-registered baseline and follow-up images are fused in a single color-encoded difference image. This allows an expert reader to efficiently interpret progressive changes while focusing on just one image. Experiments in which an expert reader used the proposed framework to score inflammatory changes in axial SpA patients were performed. Results showed strong agreement with ground truth scores for cases of full lesion occurrence/remission.**

***Index Terms*—Vertebrae segmentation, MRI, comparative visualization**

I. Introduction

SPONDYLOARTHRITIS (SpA) comprises a group of related inflammatory diseases of which ankylosing spondylitis (AS) is considered the prototype. It mainly affects the sacroiliac (SI) joints and spine, but peripheral joints can be affected as well, and extra-articular manifestations can be present. Patients with axial SpA experience substantial pain, stiffness, and impaired physical function [1]. The cause of the disease is multifactorial, attributed to a combination of genetic (predominantly HLA-B27 positivity) and environmental factors [2].

Early diagnosis of axial SpA is essential, since timely initiation of treatment may significantly improve long-term prognosis, reducing the risk of heavily impairing conditions. Due to its ability to visualize inflammation, magnetic resonance imaging (MRI) of the SI joints and spine has demonstrated its value in recognizing early axial SpA [3]. In particular, the use of STIR (short tau inversion recovery) acquisition sequence enhances signal from inflammatory infiltrations, while suppressing signal from bone marrow fat, which may obscure inflammatory lesions [4].

A number of scoring systems have been proposed for manual evaluation of MRIs of the SI joints and spine [5], [6], [7], [8]. In this study, we focus on the Spondyloarthritis Research Consortium of Canada (SPARCC) scoring method of the spine [7]. The 23 vertebral unit (VU) version of the SPARCC method requires an expert reader to visually assess and score the presence of increased STIR signal in 23 VUs on multiple MRI slices, which is a labor-intensive and time-consuming task. Furthermore, to monitor progressive changes over time, the expert must manually locate and align the 23 VUs in both baseline and follow-up scans, comparing two images side-by-side.

We present a semi-automated framework for comparative visualization of inflammatory lesions in MRI of the spine in axial SpA patients. To our knowledge, this work is the first attempt to perform computer-aided comparative assessment of axial SpA inflammatory lesions. The first part of our method (Section II) localizes and segments the VUs using a fully automatic algorithm based on quasi-periodicity of vertebral column intensity profile and tissue class probability maps. The second part (Section III) uses these segmentations to align baseline and follow-up scans by deriving a locally rigid transform from a pre-computed deformable registration. To facilitate visual comparison, the co-registered baseline and follow-up images are fused in a single color-encoded difference image. This allows an expert reader to efficiently interpret progressive changes while focusing on just one image. Experiments in which an expert reader used the proposed framework to score inflammatory changes in axial SpA patients were performed. Results showed strong agreement with SPARCC scores for cases of full lesion occurrence/remission.

II. Localization and Segmentation of Vertebral Bodies

A. Related Work

Extensive research in spine localization and segmentation has been carried out in the computed tomography (CT) domain and increasing number of methods have been proposed in the MRI domain in recent years. It is important to note that localization and segmentation of vertebral bodies and

inter-vertebral discs (IVD) in MRI images is generally a more challenging task compared to CT images. This is mainly due to inherent magnetic field inhomogeneities of MRI scanners, which cause large variability in vertebral and IVD tissue signal intensity across the image. For CT images of the spine, Major *et al.* [9] propose an automated algorithm for 3D landmarking and labeling of vertebral bodies. They use probabilistic boosting trees [10] to detect the spinal canal and IVDs, and then employ a Markov random field (MRF)-based approach to obtain the final landmarks and labels. Kadoury *et al.* [11] present a 3D segmentation algorithm based on manifold embeddings and higher order MRFs. Rasoulian *et al.* [12] develop a statistical multi-object shape+pose model of lumbar spine, and employ an expectation maximization (EM) technique [13] to align the model with CT images in a semi-automatic fashion. Tan *et al.* [14] propose a semi-automatic 3D vertebra segmentation algorithm based on 3D multi-scale cascade of successive level sets. Štern *et al.* [15] use geometrical properties of vertebral bodies to extract the spinal centerline, construct an intensity profile, and apply correlation measurements to obtain a smooth quasi-periodic profile from which the locations of vertebral bodies and IVDs are estimated. In another study [16], the same authors use parametric 3D modeling to segment the vertebrae.

A variety of approaches to localization and segmentation of vertebral bodies and IVDs in MRI have been reported in literature. Jerebko *et al.* [17] fit a 4th order 3D polynomial to the spinal canal curve to construct a vertebral column intensity profile, and exploit the latter's quasi-periodic pattern to localize vertebral body centers using band-pass filtering. An active shape model is then applied to segment the vertebrae. The methods by Štern *et al.* [15], [16], discussed above, are also applied by the authors to MRI images of the spine. Peng *et al.* [18] convolve each sagittal slice with a pre-selected 20 x 40 IVD template kernel to obtain initial clues for the IVD positions. Then, slice by slice, a 4th order polynomial is fitted along the clues to construct an intensity profile, where local maxima correspond to IVD centers and distances between adjacent local maxima correspond to vertebra heights. The slice with minimal vertebral height variance is selected for further processing, where edge detection, connectivity tracing, and corner points are used to segment vertebrae in 2D. Michopoulou *et al.* [19] propose a semi-automatic 2D IVD segmentation that combines a trained probabilistic IVD atlas with the robust fuzzy *c*-means (RFCM) [20] algorithm. Shi *et al.* [21] perform semi-automatic 2D IVD segmentation by first segmenting the spinal canal based on the Hough transform and then using local window intensity statistics to locate the IVDs. A number of studies use the graph cuts framework to segment vertebral bodies. Carballido-Gamio *et al.* [22] apply normalized cuts with Nyström approximation [23] to 3D local intensity histograms to obtain 2D vertebrae segmentations. Egger *et al.* [24] propose a rectangle-based graph cut algorithm (Square-Cut) for 2D vertebrae segmentation. Huang *et al.* [25] use a modified AdaBoost algorithm [26] to detect vertebra candidates, and apply random sample consensus (RANSAC) [27] to fit a spinal curve through the vertebrae while eliminating false detections. Then, 2D vertebrae segmentations are obtained through an iterative normalized-cut algorithm.

B. Methods

The methods described below were designed for and tested on MRI data consisting of T1-weighted turbo spin echo (T1TSE) (TR 500/TE 7) and STIR (TR 2655/TE 64) sequences of the upper and lower spine acquired sagittally on a 1.5T MRI scanner (Philips Medical Systems, Best, the Netherlands) [Fig. 1]. We assume that the acquired T1-weighted and STIR volumes are co-registered. The methods were implemented in MATLAB R2012b (MathWorks, Inc.).

Our approach to fully automated 3D vertebrae segmentation in SpA MRI consists of the following steps: 1) Spinal canal segmentation; 2) Vertebral column-spinal canal boundary estimation; 3) Localization of vertebral bodies; 4) Correlation-based vertebrae segmentation.

1) Spinal Canal Segmentation: Due to high cerebrospinal fluid (CSF) content, spinal canal exhibits strong hyperintense appearance in STIR MRI images [Fig. 1(b)], what makes it a prominent reference object for localization tasks. Furthermore, the spinal canal is adjacent to the vertebral column and therefore closely resembles the latter in curvature. We exploit these properties to automatically locate and parameterize the boundary between the vertebral column and the spinal canal, with the ultimate goal of constructing a vertebral column intensity profile.

The spinal canal is best visible in its full extent around the mid-sagittal image plane. The same holds for vertebral bodies. Therefore, to segment these objects accurately, it is essential to locate a mid-sagittal reference slice. We begin by obtaining a low resolution estimate of each slice [Fig. 2(b)] in the STIR volume using an ideal low-pass filter with cutoff frequency radius $r_l = 20$. Hence, for a DFT spectrum $F[u,v]$ of a slice image, where u and v are the horizontal and vertical spatial frequency indices, respectively, the spectrum $F_l[u,v]$ after retaining low frequency components is defined as

$$F_l[u,v] = \begin{cases} F[u,v], & |u| \le r_l;\ |v| \le r_l - |u| \\ 0, & \text{otherwise} \end{cases}. \qquad (1)$$

Then, in the resulting low resolution image, we find the location of highest intensity in each row, and mark this location as "1" in a binary image that serves as a segmentation mask estimate for the spinal canal. To account for outliers and discontinuities, we apply dilation with a square structuring element of width 10, and retain the largest connected component. Fig. 2(c) shows an example of the final segmentation result overlaid on the original STIR image. Since in the mid-sagittal plane the spinal canal appears in its longest extent, the slice with the largest number of segmented points is taken as the reference slice for all further processing.

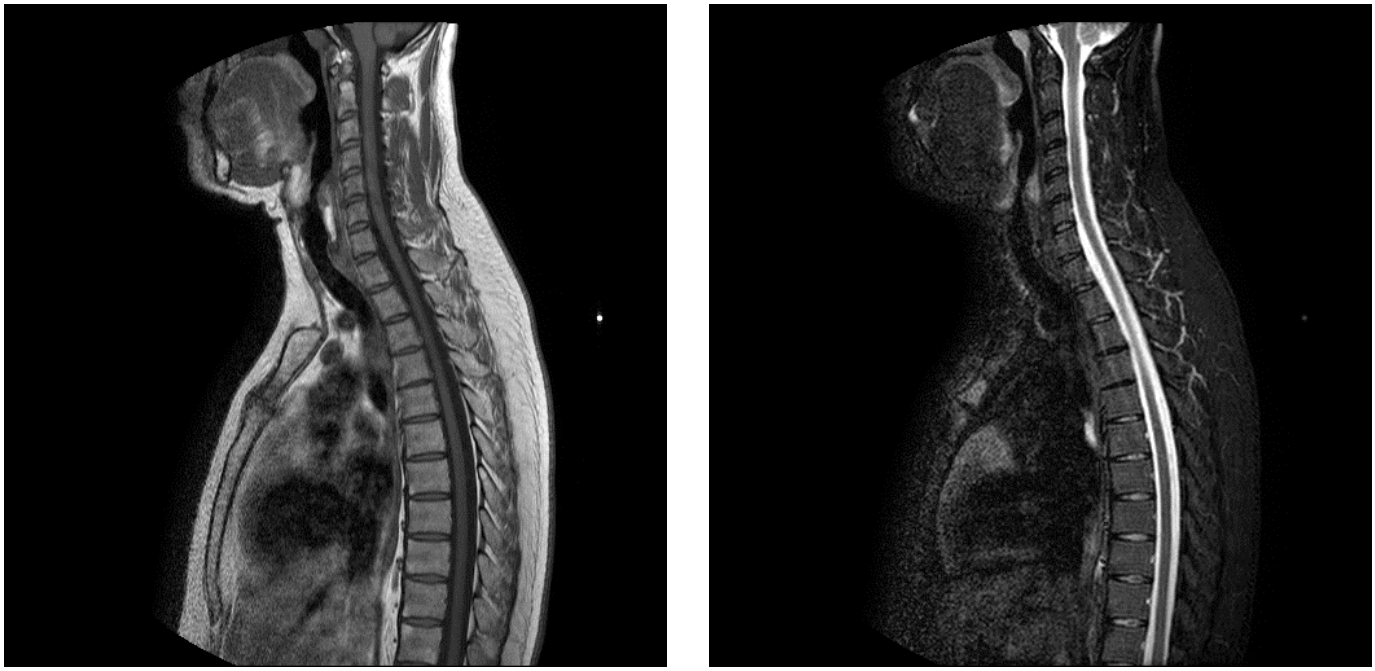

(a) (b)

Fig. 1. MRI images of the spine. (a) T1-weighted. (b) STIR.

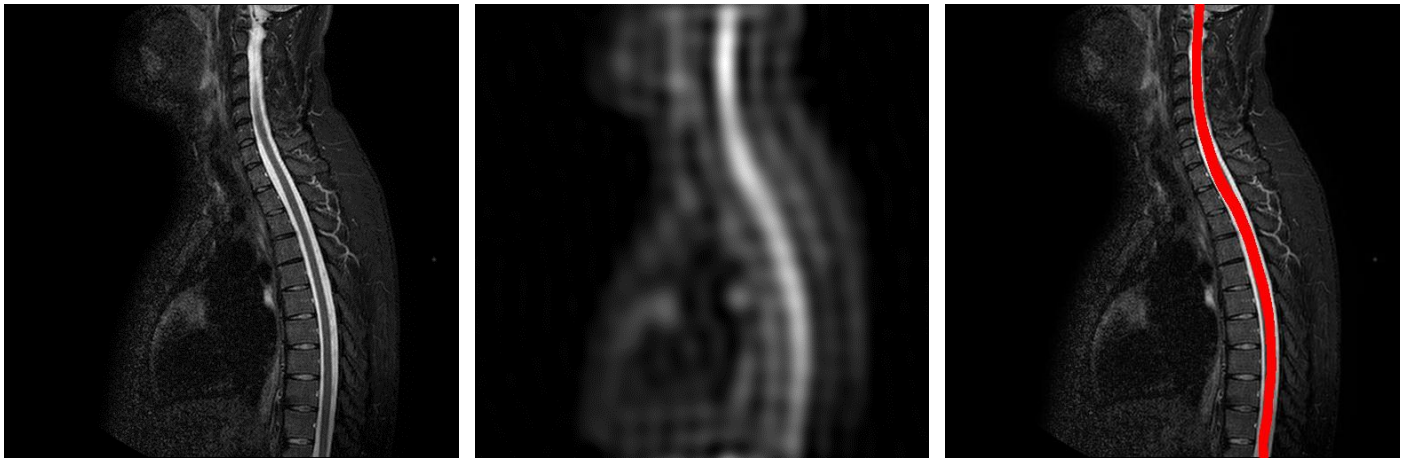

(a) (b) (c)

Fig. 2. Spinal canal segmentation. (a) Original STIR image. (b) Low spatial frequency estimate of (a). (c) Final segmentation result overlaid on (a).

2) Vertebral Column-Spinal Canal Boundary Estimation: Having segmented the spinal canal, we have closely approached the vertebral column, which is the ultimate image region of interest. In order to further lock down on the latter's location, we exploit the spinal canal's proximity and curvature resemblance to the vertebral column to estimate the boundary between these two structures. First, the horizontal gradient $G_{x,\,ref}$ is computed over the STIR reference slice image I_{ref}^{STIR} (the gradient is computed simply as the intensity difference between horizontally adjacent pixels). To restrict the region of interest, we define $G'_{x,\,ref}$, given by

$$G'_{x,\,ref}(x,y)=\begin{cases} G_{x,\,ref}(x,y), & c_l-10\le x\le c_r+10 \\ 0 & \text{, otherwise} \end{cases}, \qquad (2)$$

where c_l and c_r are the left-most and right-most segmented columns in the spinal canal segmentation mask image. An example of $G'_{x,\,ref}$ is shown in Fig. 3(a). Notice that the boundary between the vertebral column and the spinal canal is characterized by a strong positive edge. Therefore, to further prune the gradient image, only positive-valued gradient locations are retained [Fig. 3(b)], yielding

$$G'^{+}_{x,ref}(x,y)=\max\left(G'_{x,\,ref}(x,y),\ 0\right). \qquad (3)$$

To obtain a robust estimate of the boundary outline, we now exploit the close similarity in curvature between the latter and the spinal canal segmentation. Let s_c denote the skeleton of

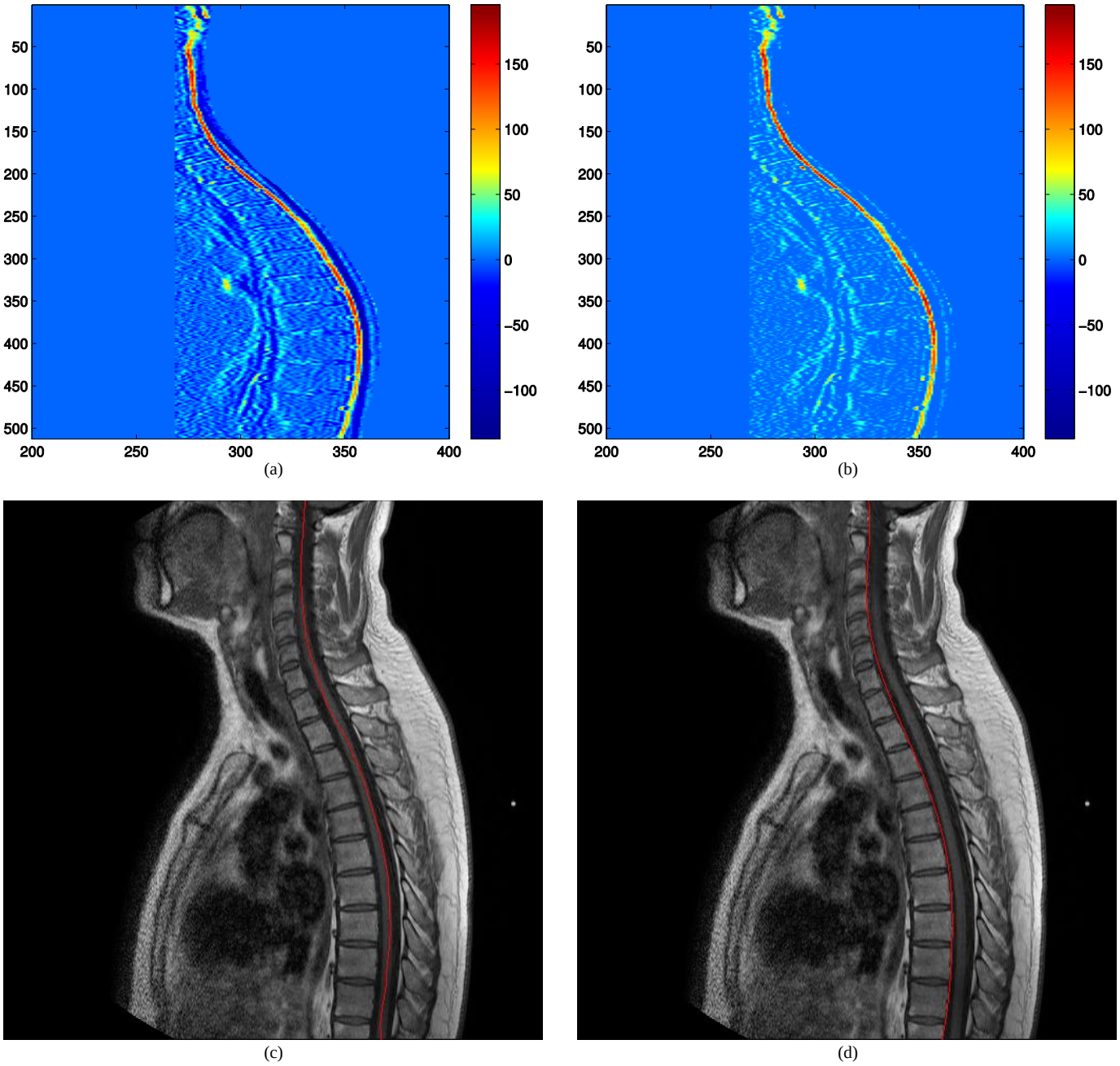

Fig. 3. Vertebral column-spinal canal boundary estimation. (a) Horizontal gradient image $G'_{x,ref}$ of the reference STIR slice after discarding regions to the left and to the right of the spinal canal. (b) Positive-valued horizontal gradient $G'^{+}_{x,ref}$. (c) Skeleton s_c of spinal canal segmentation overlaid on T1-weighted image. (d) 7th order polynomial p_b final approximation to vertebral column-spinal canal boundary, overlaid on T1-weighted image.

the spinal canal segmentation mask, obtained by retaining the middle segmented pixel in each row [Fig. 3(c)]. By computing 2D cross-correlation between $G'^{+}_{x,ref}$ and s_c and finding the spatial location of maximal correlation, we estimate the horizontal distance d_s between the mask in s_c and the positive gradient edge in $G'_{x,ref}$. The first approximation to the vertebral column-spinal canal boundary is then obtained by horizontally shifting s_c to the left by d_s pixels. Subsequently, the shifted mask is dilated with a square structuring element of width 10. For each row, the pixel location corresponding to maximal $G'^{+}_{x,ref}$ value lying within the dilated mask is retained, yielding a second approximation to the boundary. Finally, to account for discontinuities and outliers, a 7th order polynomial p_b is fitted to candidate boundary points, providing a smooth, continuous approximation of the boundary [Fig. 3(d)]. For a given row y, the column index of the boundary is given by $x = p_b(y)$.

3) Localization of Vertebral Bodies: Now that we obtained a one-sided outline of the vertebral column, we are well-equipped to compute the vertebral column intensity profile. All processing steps in this sub-section are performed on the T1-weighted reference slice image, denoted by I_{ref}^{T1}. T1-weighted images of the spine are characterized by a consistent alternating pattern of high-low-high signal intensity as one traces the intensity along the superior-inferior extent of the vertebral column. Higher intensities correspond to vertebral bodies, while lower intensities correspond to IVDs. Therefore, by computing the profile of image intensity along the entire vertebral column, it is possible to estimate the locations of vertebral bodies and IVDs as the locations of corresponding intensity profile extrema.

Our approach to computation of the intensity profile builds upon the method introduced by Jerebko *et al.* [17], and introduces several innovations. First, we note that for a given point $(p_b(y), y)$ on the vertebral column-spinal canal boundary, the direction normal to the boundary at that point covers an anatomically consistent part of the vertebral column. It is consistent in the sense that if $(p_b(y), y)$ lies on the boundary of a vertebral body (or IVD), pixels lying along the respective normal direction to p_b at that point, belong to the same vertebral body (or IVD). Hence, by considering each boundary point $(p_b(y), y)$ and averaging image intensity along the respective normal direction to p_b, we can construct a vertebral column intensity profile $h(y)$, where each value of y corresponds to a specific vertebral body (or IVD).

To compute the directions normal to p_b at every value of y in a robust manner, the boundary curve is first divided into segments of $(\Delta_b + 1)$ points. Here, we take $\Delta_b = 20$. For a given interval $[y_1, y_2]$, where $y_2 = y_1 + \Delta_b$, the normal vector to p_b is computed as

$$\vec{n}_{y_1,y_2} = \frac{\vec{\tilde{n}}_{y_1,y_2}}{\left\| \vec{\tilde{n}}_{y_1,y_2} \right\|_2}, \tag{4}$$

where $\vec{\tilde{n}}_{y_1,y_2} = \begin{pmatrix} 0 & -1 \\ 1 & 0 \end{pmatrix} \begin{bmatrix} p_b(y_2) - p_b(y_1) \\ \Delta_b \end{bmatrix}$ and $\|\cdot\|_2$ denotes the L_2-norm of a vector. The left matrix in the above equation is the well-known rotation matrix evaluated at rotation angle $\theta = 90^\circ$. Simply put, the operation above rotates a vector that is approximately tangent to p_b in the short interval $[y_1, y_2]$ by 90 degrees, yielding a vector that is approximately normal to p_b in the same interval. Now, for a given value of $y \in [y_1, y_2]$, the corresponding vertebral column intensity profile value $h(y)$ is computed as the intensity average of $(M+1)$ points (here, we take $M = 20$) taken along the normal direction defined by $\vec{n}_{y_1,y_2}$:

$$h(y) = \frac{1}{M+1} \sum_{m=0}^{M} I_{ref}^{T1}(x_m, y_m), \tag{5}$$

where $\begin{bmatrix} x_m \\ y_m \end{bmatrix} = \begin{bmatrix} p_b(y) \\ y \end{bmatrix} + m \cdot \vec{n}_{y_1,y_2}$. For those values of y where $h(y)$ depends on pixel locations outside the image borders, $h(y)$ is interpolated to the nearest existing $h(y)$ value. Fig. 4(a) shows the resulting vertebral column intensity profile for the T1-weighted image in Fig. 3.

As illustrated in Fig. 4(a), the profile signal computed from (5) exhibits the desired pattern of alternating high and low intensities corresponding to vertebral bodies and IVDs, but is very noisy. To localize the vertebral bodies, we seek a smooth profile with alternating local maxima/minima that correspond to alternating vertebral bodies/IVDs, respectively. First, as proposed in [17], to filter out high intensity spurs (for example, at IVD locations) that may induce errors during subsequent processing steps, we apply a minimum-rank filter to the profile signal. The output signal is denoted as $h_f(y)$. The filtering operation is performed by sliding a window across the profile and assigning the output value to the minimal input value inside the window. It is therefore suggested in [17] to choose a window length that is larger than the largest distance between two adjacent vertebrae and smaller than the height of the shortest vertebra. Here, we use a window length of 5 points. Fig. 4(b) shows the result of applying minimum-rank filtering to the intensity profile in Fig. 4(a).

To compensate for intensity inhomogeneity effects, we split the profile into four segments $w_{1,\ldots,4}$ of equal length and vertically shift the signal to obtain

$$h_s(y) = h_f(y) - \frac{(w_{\max} + w_{\min})}{2}, \; y \in [y_a, y_b], \tag{6}$$

where $w_{\max} = \max_{y \in [y_a, y_b]} \{h(y)\}$, $w_{\min} = \min_{y \in [y_a, y_b]} \{h(y)\}$, and y_a, y_b are the boundary indices of segment w_i $(i = 1, \ldots, 4)$. To normalize signal intensity, h_s is scaled and shifted to range $[-1, 1]$:

$$\bar{h}_s(y) = 2 \cdot \frac{h_s(y) - \min_{y \in [y_a, y_b]} \{h_s(y)\}}{\max_{y \in [y_a, y_b]} \{h_s(y)\} - \min_{y \in [y_a, y_b]} \{h_s(y)\}} - 1, \tag{7}$$

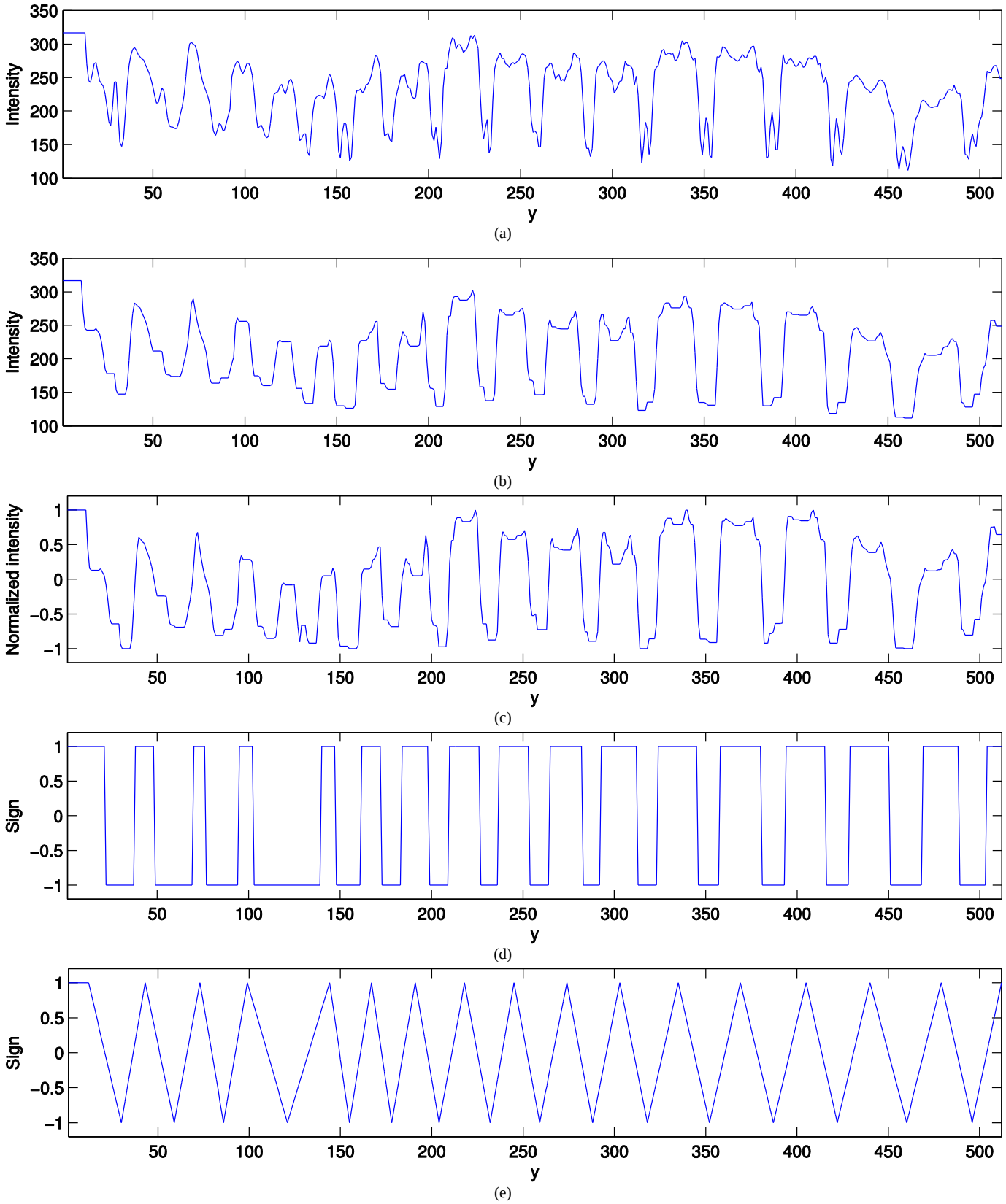

Fig. 4. Vertebral column intensity profile. (a) Raw profile signal h. (b) Minimum-rank filtered profile h_f. (c) Normalized profile $\bar{h}_s$. (d) Sign sequence h_{sgn} of normalized profile $\bar{h}_s$. (e) Piecewise linear approximation $\tilde{h}_{\text{sgn}}$ to sign sequence h_{sgn}.

where $y \in [y_a, y_b]$. The result of applying normalization is shown in Fig. 4(c).

In order to further smooth the profile signal, we will exploit the latter's quasi-periodic pattern. It is apparent from Fig. 4(c) that this oscillatory pattern is a superposition of a group of harmonics of similar frequencies. As in [17], we seek to retain only those frequency components that describe the smooth oscillatory pattern. In their work, Jerebko *et al.* retain a fixed frequency band derived from the height range of normal vertebrae. Here, we take a different approach, adapting the frequency band to the specific image at hand. First, we compute the sign function of $\bar{h}_s(y)$ [Fig. 4(d)]:

$$h_{\text{sgn}}(y) = \text{sgn}\left(\bar{h}_s(y)\right). \tag{8}$$

Now, let $Y_t = \left\{ y_{t,i} : h_{\text{sgn}}(y_{t,i}) \neq h_{\text{sgn}}(y_{t,i}-1) \right\} \quad (i = 1,...,L)$ denote the set of locations at which sign transitions occur in h_{sgn}, where L is the total number of sign transitions. Next, we compute a piecewise linear approximation to h_{sgn}:

$$\tilde{h}_{\text{sgn}}(y) = \begin{cases} \tilde{h}_{\text{sgn}}(y_{\alpha,l}) + m_t \cdot (y - y_{\alpha,l}) & , y > y_{\alpha,0} \\ h_{\text{sgn}}(y) & , y \le y_{\alpha,0} \end{cases}, \tag{9}$$

where the parameters are defined as:

$$y_{\alpha,l} = y_{t,l} + \text{round}\left((y_{t,l+1} - y_{t,l})/2\right);$$
$$y_{\alpha,0} = \text{round}\left(y_{t,1}/2\right) + 1;$$
$$m_t = \frac{h_{\text{sgn}}(y_{\alpha,l}) - h_{\text{sgn}}(y_{\alpha,l-1})}{y_{\alpha,l} - y_{\alpha,l-1}};$$
$$l = \arg\min_i \left\{ \left| y_{t,i} - y \right| \right\}, \text{ subject to: } y_{t,i} < y;$$
$$y_{t,i} \in Y_t; \quad i = 1,...,L.$$

Effectively, we linearly interpolate the sign sequence between consecutive mid-points of constant sign value. The motivation behind this operation is to obtain a signal with well-defined local extrema [Fig. 4(e)]. This property makes $\tilde{h}_{\text{sgn}}$ more similar to a band-pass signal, rather than the approximately rectangular pulse-shaped normalized profile $\bar{h}_s$. In turn, this will now allow us to determine the band of frequencies describing a smooth approximation to $\bar{h}_s$. Let $\tilde{H}_{\text{sgn}}[k]$ and $\bar{H}_s[k]$ denote the DFTs of $\tilde{h}_{\text{sgn}}(y)$ and $\bar{h}_s(y)$, respectively. Further, let $\bar{H}_s^{k_{BL}}[k]$ denote a band-limited version of $\bar{H}_s[k]$ defined as

$$\bar{H}_s^{k_{BL}}[k] = \begin{cases} \bar{H}_s[k] & , |k| \le k_{BL} \\ 0 & , |k| > k_{BL} \end{cases}. \tag{10}$$

Let us now compute the inverse DFT of $\bar{H}_s^{k_{BL}}[k]$, denoted as $\bar{h}_s^{k_{BL}}(y)$, for $k_{BL} = 0,...,50$, and for each value of k_{BL} evaluate the mean squared error (MSE) between $\bar{h}_s^{k_{BL}}(y)$ and the piecewise linear signal $\tilde{h}_{\text{sgn}}(y)$:

$$e_{MSE}(k_{BL}) = \frac{1}{N_y} \sum_{y=0}^{N_y - 1} \left(\tilde{h}_{\text{sgn}}(y) - \bar{h}_s^{k_{BL}}(y) \right)^2, \tag{11}$$

where N_y is the length of the profile signal. To smooth the error sequence, e_{MSE} is convolved with a moving average filter of length 5. The result is shown in Fig. 5. Note the

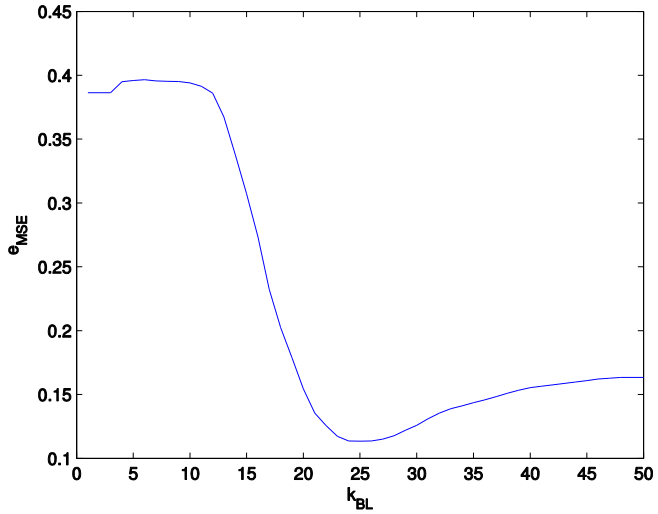

Fig. 5. Mean squared error e_{MSE} between band-limited normalized profile $\bar{h}_s^{k_{BL}}$ and piecewise linear profile approximation $\tilde{h}_{\text{sgn}}$ as a function of band-limiting frequency k_{BL}.

sharp decrease in error towards a global minimum around $k_{BL} = 25$ and the subsequent monotonic increase as k_{BL} increases. To understand this trend, let us recall again that $\tilde{h}_{\text{sgn}}$ exhibits band-pass behavior with well-defined local extrema, while $\bar{h}_s$ is characterized by approximately rectangular pulse shape. As k_{BL} begins to increase, local extrema of $\bar{h}_s^{k_{BL}}$ start to align with local extrema of $\tilde{h}_{\text{sgn}}$. This alignment is most accurate for values of k_{BL} yielding the minimal e_{MSE}. However, as k_{BL} increases further, local extrema of $\bar{h}_s^{k_{BL}}$ begin to split into multiple neighboring minima/maxima and the width of each original pulse increases [Fig. 6] as the band-limited signal approaches its full-band appearance of Fig. 4(c).

To precisely define the frequency band used for profile smoothing, we empirically choose a value of $k_{BL} = k_{FB}$ in the left-sided vicinity of the global minimum of e_{MSE}:

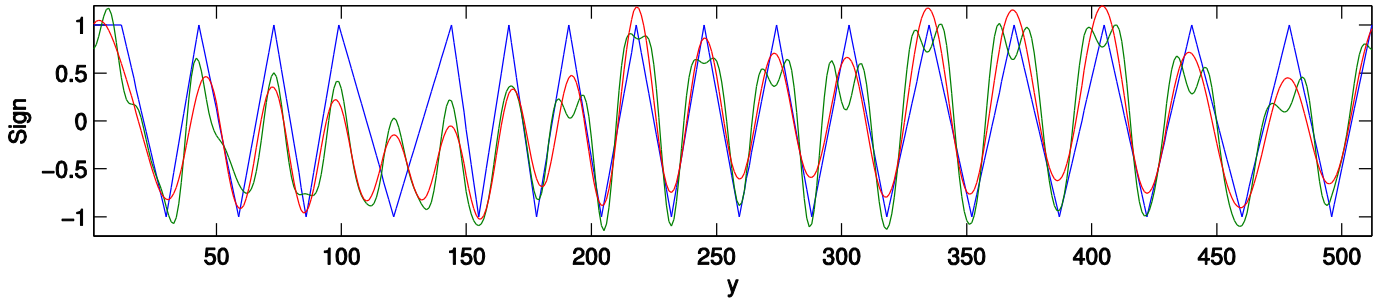

Fig. 6. Comparison between $\tilde{h}_{sgn}$ (blue) and $\bar{h}_{s}^{k_{BL}}$ for $k_{BL} = 24$ (red) and $k_{BL} = 50$ (green).

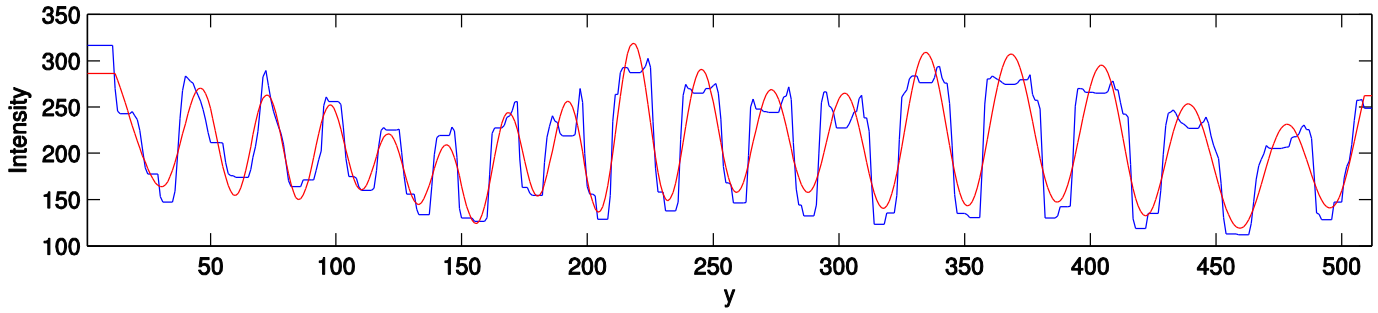

Fig. 7. Smooth approximation to the vertebral column intensity profile. Minimum-rank filtered profile signal h_f (blue), smooth approximation signal $\tilde{h}_f^{k_{FB}}$ (red).

$$k_{FB} = \arg\min_{k_{BL}} \left\{ \left| e'_{MSE}(k_{BL}) - 0.1 \cdot \min\left\{ e'_{MSE}(k_{BL}) \right\} \right| \right\}, \quad \text{subject to } k_{BL} > \arg\min_{k_{BL}} \left\{ e'_{MSE}(k_{BL}) \right\}, \tag{12}$$

where $e'_{MSE}(k_{BL})$ denotes the derivative of e'_{MSE} with respect to k_{BL}. The smooth approximation to the vertebral column profile is now obtained by band-limiting the minimum-rank filtered profile signal h_f with the frequency band defined by k_{FB}. Let $H_f[k]$ denote the DFT of $h_f(y)$. The DFT spectrum of the smooth approximation is then given by:

$$\tilde{H}_f^{k_{FB}}[k] = \begin{cases} H_f[k], & |k| \le k_{FB} \\ 0, & |k| > k_{FB} \end{cases} \tag{13}$$

and the approximation profile $\tilde{h}_f^{k_{FB}}(y)$ is obtained by computing the inverse DFT of $\tilde{H}_f^{k_{FB}}[k]$. We make sure that edge regions (left and right extremes) of $\tilde{h}_f^{k_{FB}}$ are consistent with h_f by setting edge values in the interval where h_f is constant to the nearest value of $\tilde{h}_f^{k_{FB}}$ outside this constant interval. Fig. 7 shows the smooth approximation signal (red) overlaid on the original filtered profile (blue). Note that $\tilde{h}_f^{k_{FB}}$ does indeed exhibit the desired property of well-localized local extrema. Moreover, these local extrema are typically centered around the mid-point of the original signal's peaks and valleys, which correspond to vertebral bodies and IVDs, respectively. Therefore, by determining the locations of all local maxima/minima of $\tilde{h}_f^{k_{FB}}$, we will localize the vertebral bodies/IVDs in the image. Since the signal is very smooth, this is done simply by computing the derivative of $\tilde{h}_f^{k_{FB}}$ and detecting locations of derivative sign change. Let $Y_{vert}^0 = \left\{ y_{v_0,1}, ..., y_{v_0,N_v} \right\}$ and $Y_{disc}^0 = \left\{ y_{d_0,1}, ..., y_{d_0,N_d} \right\}$ denote the sets of y coordinates corresponding to local maxima and minima of $\tilde{h}_f^{k_{FB}}$, respectively. N_v and N_d are equal to the total number of elements in Y_{vert}^0 and Y_{disc}^0, respectively. To complete the vertebral body localization task, we need to assign to each detection in Y_{vert}^0 a coordinate pair (x, y) lying to the left of the vertebral column boundary p_b. Let $X_{vert} = \left\{ x_{v,1}, ..., x_{v,N_v} \right\}$ and $Y_{vert} = \left\{ y_{v,1}, ..., y_{v,N_v} \right\}$ denote the set of (x, y) coordinates of vertebral bodies corresponding to the detections in Y_{vert}^0, which are given by:

$$\begin{bmatrix} x_{v,i} \\ y_{v,i} \end{bmatrix} = \begin{bmatrix} p_b(y_{v_0,i}) \\ y_{v_0,i} \end{bmatrix} + m \cdot \vec{n}_{y_1,y_2}, \tag{14}$$

where $\vec{n}_{y_1,y_2}$ is defined by (4) with $y_1 = y_{v_0,i}$, $y_2 = y_1 + 5$, and $m = \left| y_{v_0,i} - y_{d_0,i} \right|$. Fig. 8 shows the resulting vertebral body localization for upper and lower spine images.

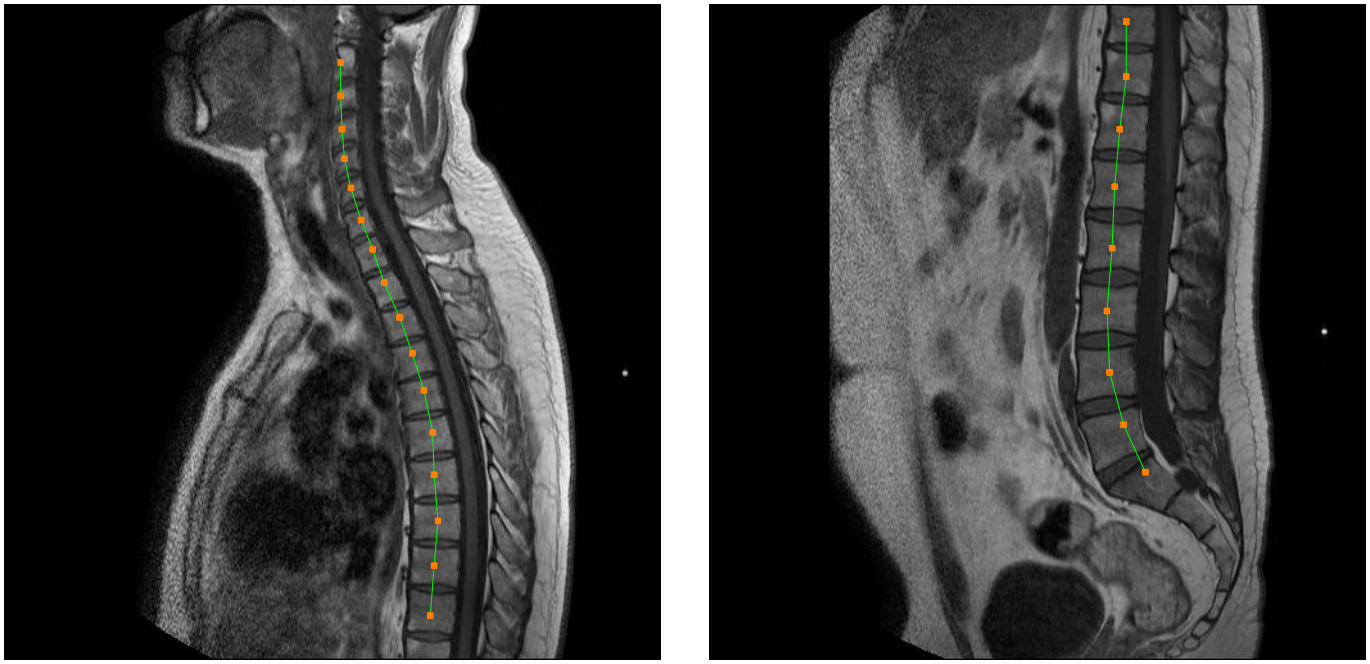

(a) (b)

Fig. 8. Localization of vertebral bodies. (a) Upper spine. (b) Lower spine.

4) Correlation-Based Vertebrae Segmentation: Now that the locations of vertebral bodies have been determined, we are ready to proceed to the segmentation task. To facilitate segmentation by decreasing signal variability within the vertebral tissue, we use the method by Dzyubachyk et al. [28] for joint intensity inhomogeneity correction to extract 5 discrete tissue class probability maps based on the joint intensity distribution of the T1-weighted and STIR MRI volumes. The tissue classes are 1) air, 2) vasculature, 3) fat, 4) muscle, 5) fluid. Since vertebral bodies do not contain muscle tissue, voxel values within vertebrae in the muscle tissue probability map $I_M^P(x,y,z)$ are close to 0 and exhibit low variance. For convenience, we compute the complement of muscle probability, $\bar{I}_M^P(x,y,z)=1-I_M^P(x,y,z)$, thereby making voxel values within vertebral bodies close to 1 [Fig. 9(a, c)]. Next, to simplify navigation within the vertebral column space during subsequent processing, we compute a stretched curved planar reformation (CPR) [29] view of $\bar{I}_M^P$ along the boundary curve $p_b(y)$ [Fig. 9(b, d)]. In CPR view, denoted as $q(x_q,y_q,z)$, the vertical dimension, y_q, corresponds to positions along the boundary curve p_b, while the horizontal dimension, x_q, corresponds to the orthogonal direction to p_b. Note that in CPR view, the left and right directions are flipped with respect to $\bar{I}_M^P$. The mechanics of computing the CPR view are already in place from (4) and (5). The difference from (5) is that here we do not average the image along the orthogonal direction, but rather simply record the voxel value at distance m from the vertebral column boundary. This is done for $m=1,...,90$. Effectively, the CPR view displays a set of non-averaged vertebral column intensity profiles at a range of distances from the vertebral column-spinal canal boundary. These computations are done for each slice within the volume $\bar{I}_M^P$, with p_b always taken from the reference slice. Further, in preparation for segmentation, we convolve each slice of the CPR volume with a 5×5 Gaussian filter of standard deviation $\sigma=10$, obtaining $q^{SM}(x_q,y_q,z)$. In the following steps, we will approximate the region belonging to a vertebral body in the CPR slice images with a rectangular mask, which is equivalent to a polygon in the original image space.

Let us now consider the reference slice of $\bar{I}_M^P$ in CPR view, given by $q_{ref}^{SM}(x_q,y_q)=q^{SM}(x_q,y_q,z_{ref})$, where z_{ref} is the reference slice index. The following processing steps are repeated for each vertebral body. Consider the vertebra corresponding to $y_{v_0,i}\in Y_{vert}^0$, $i=1,...,N_v$. Let us focus on the region vertically bounded by the IVDs adjacent to the vertebra, i.e. $y_{d_0,i-1}\le y_q\le y_{d_0,i}$ and horizontally bounded by the distance $2\cdot\left|y_{v_0,i}-y_{d_0,i}\right|$. We average the region along the horizontal dimension, obtaining a 1D vertical profile of the vertebral body [Fig. 10]. Notice that the upper and lower boundaries of the vertebra are well-defined by the maximal and minimal derivative values, respectively. The vertical locations of these values are taken as estimates of vertebra's top and bottom boundaries, $y_{q,top}$, $y_{q,bot}$, respectively. To determine the horizontal extent of the vertebral body, we exploit the quasi-sinusoidal nature of the smooth vertebral column profile approximation. This time, we compute the approximation over the probability muscle image, yielding

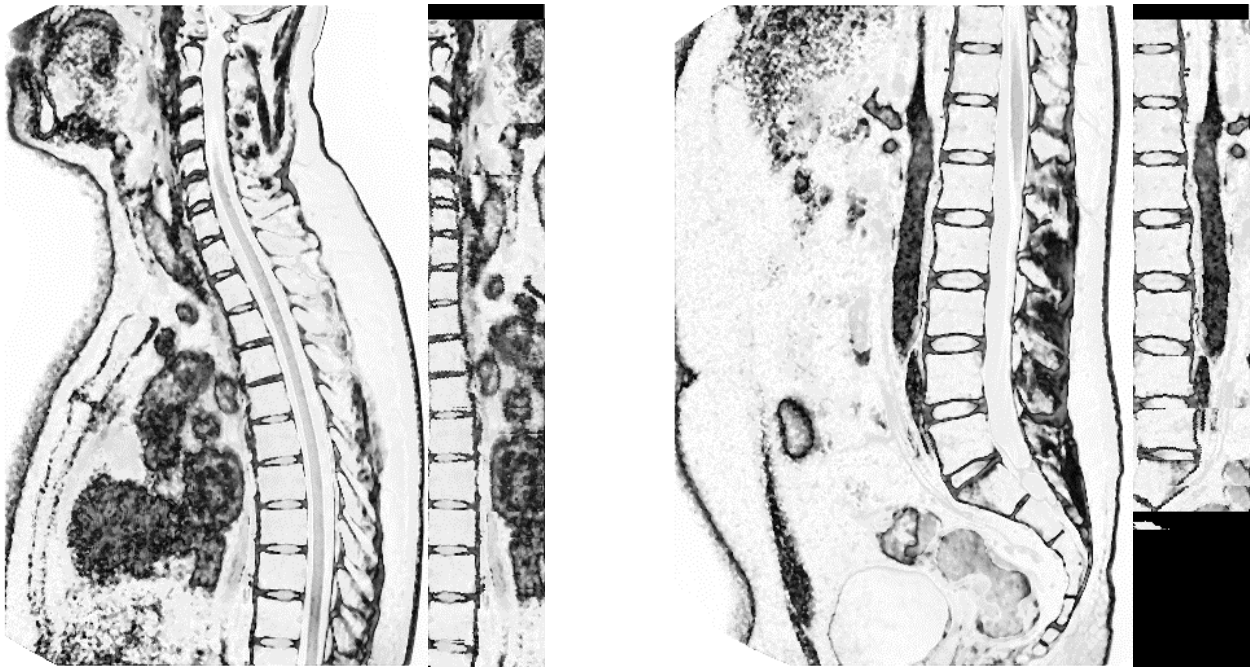

(a) (b) (c) (d)

Fig. 9. Complement of muscle tissue probability map and curved planar reformation view of the spine. (a) Upper spine. (b) CPR view of (a). (c) Lower spine. (d) CPR view of (c).

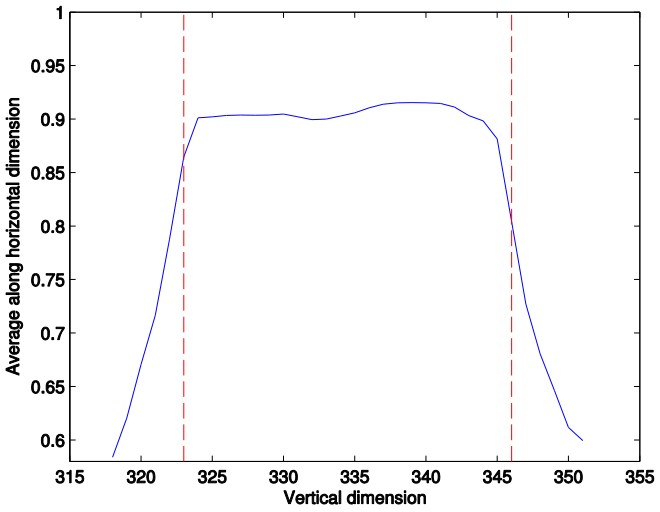

Fig. 10. Vertical profile of a vertebral body in CPR view (blue), with the estimated upper and lower boundaries $y_{q,top}$, $y_{q,bot}$ (dashed red).

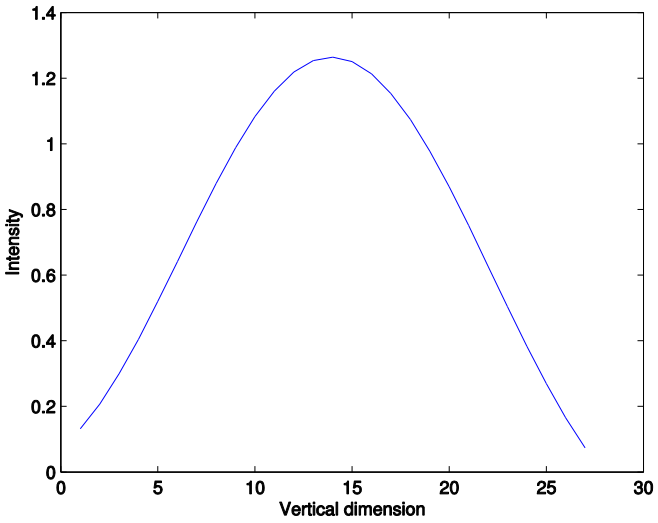

Fig. 11. Vertical profile of a vertebral body in the smooth approximation vertebral column profile signal.

$\tilde{h}_M^{k_{FB}}(y_q)$. As noted earlier, the CPR image q_{ref}^{SM} can be regarded as a collection of vertebral column intensity profiles. Therefore, it is valid to apply the smooth approximation technique of Section II-B3 to each column of q_{ref}^{SM} using (13), yielding $\tilde{q}_{ref}^{SM}$. Repeating this step for each slice of CPR volume q^{SM} produces $\tilde{q}^{SM}$. The frequency band defined by k_{FB} remains fixed during these computations. Consider now the signal $\tilde{h}_M^{k_{FB}}(y_q)$ in the interval $y_q \in [y_{q,top}, y_{q,bot}]$ [Fig. 11] and the corresponding space within $\tilde{q}_{ref}^{SM}$ [Fig. 12]. Notice from Fig. 12 that along the horizontal dimension, the pulses representing the vertebral body are in-phase with respect to each other and in-phase with respect to the pulse in Fig. 11 up to a distance corresponding to the horizontal extent of the vertebral body. To determine this distance, we compute the phase correlation of columns $x_q = 0,...,2\cdot\left|y_{v_0,i} - y_{d_0,i}\right|$ in $\tilde{q}_{ref}^{SM}$ with respect to $\tilde{h}_M^{k_{FB}}(y_q)$ in the vertical interval $y_q \in [y_{q,top}, y_{q,bot}]$. Then, we compute the real part of the

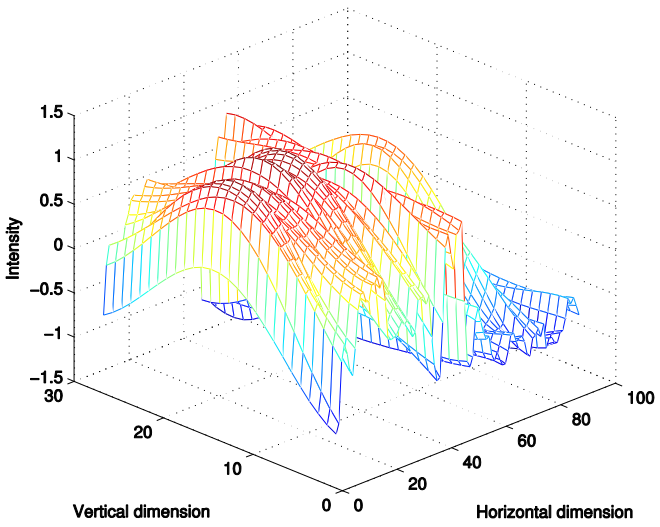

Fig. 12. Vertebral body in CPR topographic view after applying profile signal smoothing to each column of the CPR image.

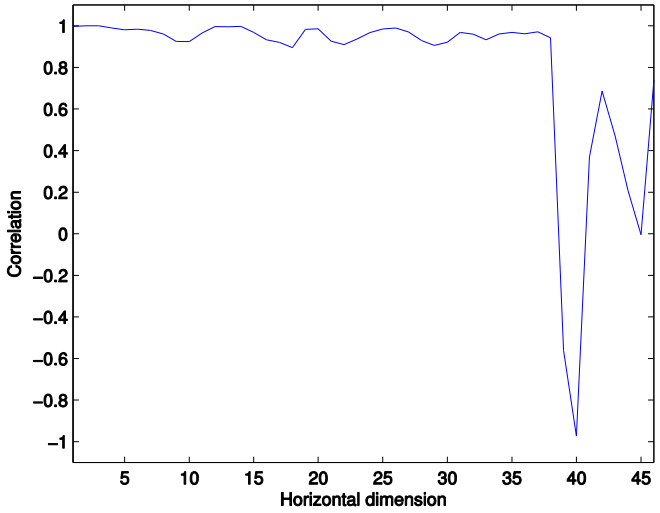

Fig. 13. Correlation of vertebral body profiles in horizontal dimension.

result evaluated at frequency $k_{v,\max} = \arg\max_k \left\{ \left| \tilde{H}_{M,v}[k] \right| \right\}$, where $\tilde{H}_{M,v}[k]$ is the DFT of $\tilde{h}_M^{k_{FB}}(y_{q,top} \ldots y_{q,bot})$. The result is shown in Fig. 13. We measure the longest interval in which the correlation is greater than threshold value $\tau_x = 0.7$ and take the end-point of this interval as the right horizontal boundary $x_{q,right}$ of the vertebral body. The left horizontal boundary is set to $x_{q,left} = 0$.

To extend the above boundary measurements to other slices in the volume, we exploit the fact that the horizontal extent of a vertebral body decreases as we move away from the reference mid-sagittal slice in either direction, while the vertical boundary does not change significantly. For each column $x_q = x_{q,left}, \ldots, x_{q,right}$ and each slice z, we measure the phase correlation at $k_{v,\max}$ between $\tilde{q}_{ref}^{SM}(x_q, y_{q,top} \ldots y_{q,bot})$ and $\tilde{q}^{SM}(x_q, y_{q,top} \ldots y_{q,bot}, z)$. For every value of x_q, we determine the slice interval around z_{ref} for which the correlation is greater than threshold value $\tau_z = 0.95$. Let $z_l(x_q)$ and $z_u(x_q)$ denote the lower and upper bounds of this interval, respectively. This way, for every horizontal coordinate $x_q = x_{q,left}, \ldots, x_{q,right}$ within the vertebral body, we assign a spatial extent interval $[z_l(x_q) - 1,\ z_u(x_q) + 1]$ in which that segment of the vertebral body is still visible in the z direction. Then for each slice $z = 0, \ldots, N_z - 1$, we find the largest value of x_q for which slice z is within the spatial extent interval $[z_l(x_q) - 1,\ z_u(x_q) + 1]$, yielding the estimate of the horizontal extent $x_{right}(z)$ at slice z:

$$x_{right}(z) = \max\{x_q\} \quad \text{subject to } z_l(x_q) - 1 \le z \le z_u(x_q) + 1. \tag{15}$$

Finally, as a safeguard from leaking into lateral spaces outside the vertebral bodies, we perform spatial correlation measurements over all vertebral bodies at once. For every horizontal coordinate $x_q = x_{q,left}, \ldots, x_{q,\max}$, where $x_{q,\max}$ is equal to the farthest right boundary x_{right} among all vertebrae in $\tilde{q}_{ref}^{SM}$, and every slice $z = 0, \ldots, N_z - 1$, we compute the spatial correlation between $\tilde{q}_{ref}^{SM}(x_q, 0 \ldots N_y - 1)$ and $\tilde{q}^{SM}(x_q, 0 \ldots N_y - 1, z)$. The correlation values are then averaged across the horizontal dimension x_q [Fig. 14]. This provides a measure of the entire vertebral column visibility as a function of slice index z. We determine the interval around reference slice z_{ref} where averaged correlation is greater than 0.75. Let z_L and z_U denote the lower and upper bounds of this interval, respectively. We define the subsequent vertebrae segmentations to be valid only for slices $z_L - 1 \le z \le z_U + 1$ and not exist outside of this interval.

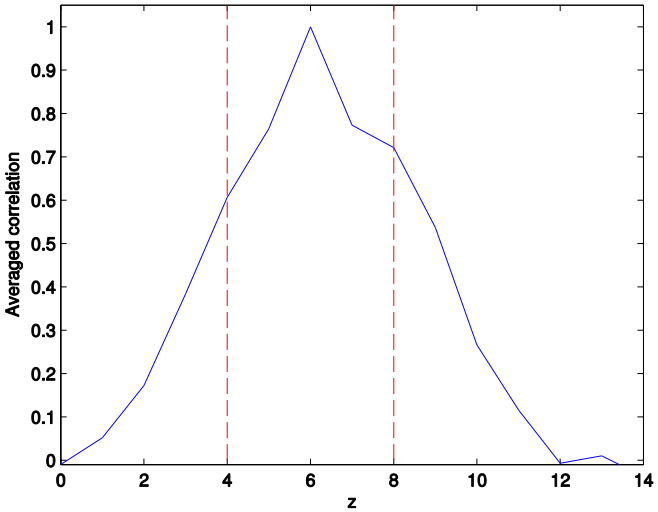

Fig. 14. Horizontally-averaged spatial correlation (blue) of the entire vertebral column profile as a function of slice index with the estimated lower and upper bounds z_L, z_U (dashed red) of the interval for which segmentation results are defined.

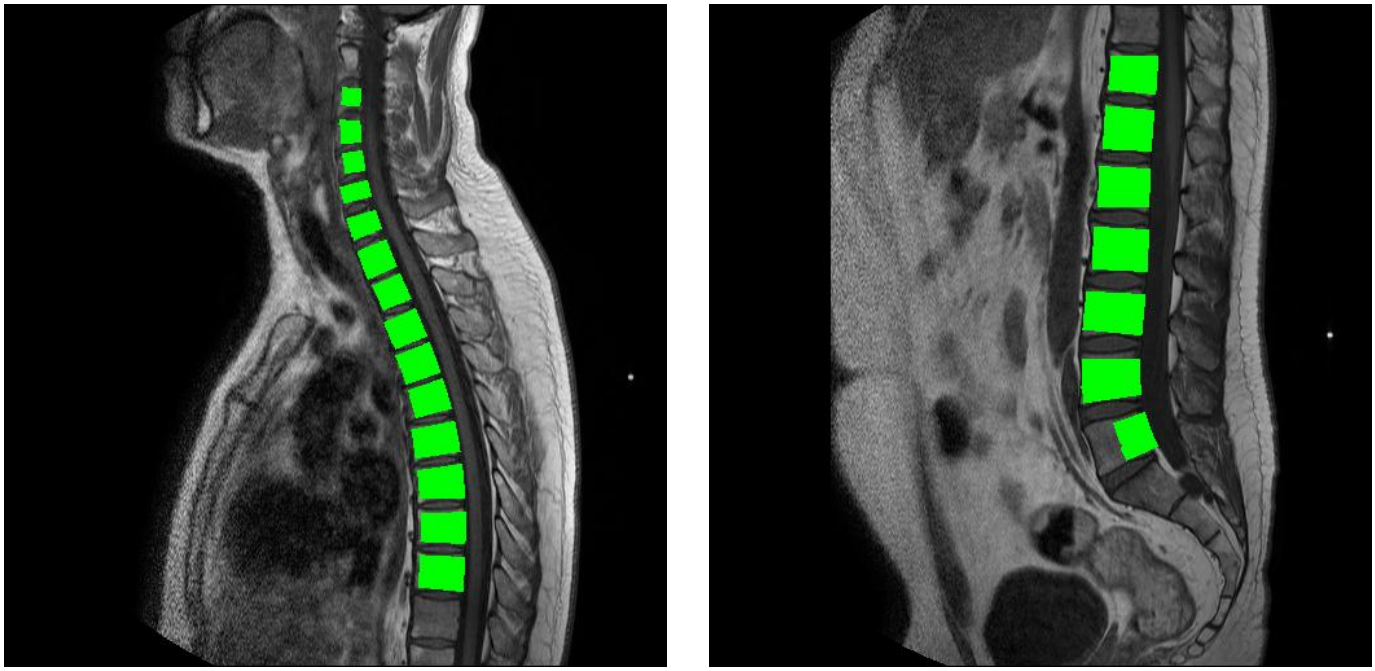

(a) (b)

Fig. 15. Segmentation of vertebral bodies. (a) Upper spine. (b) Lower spine.

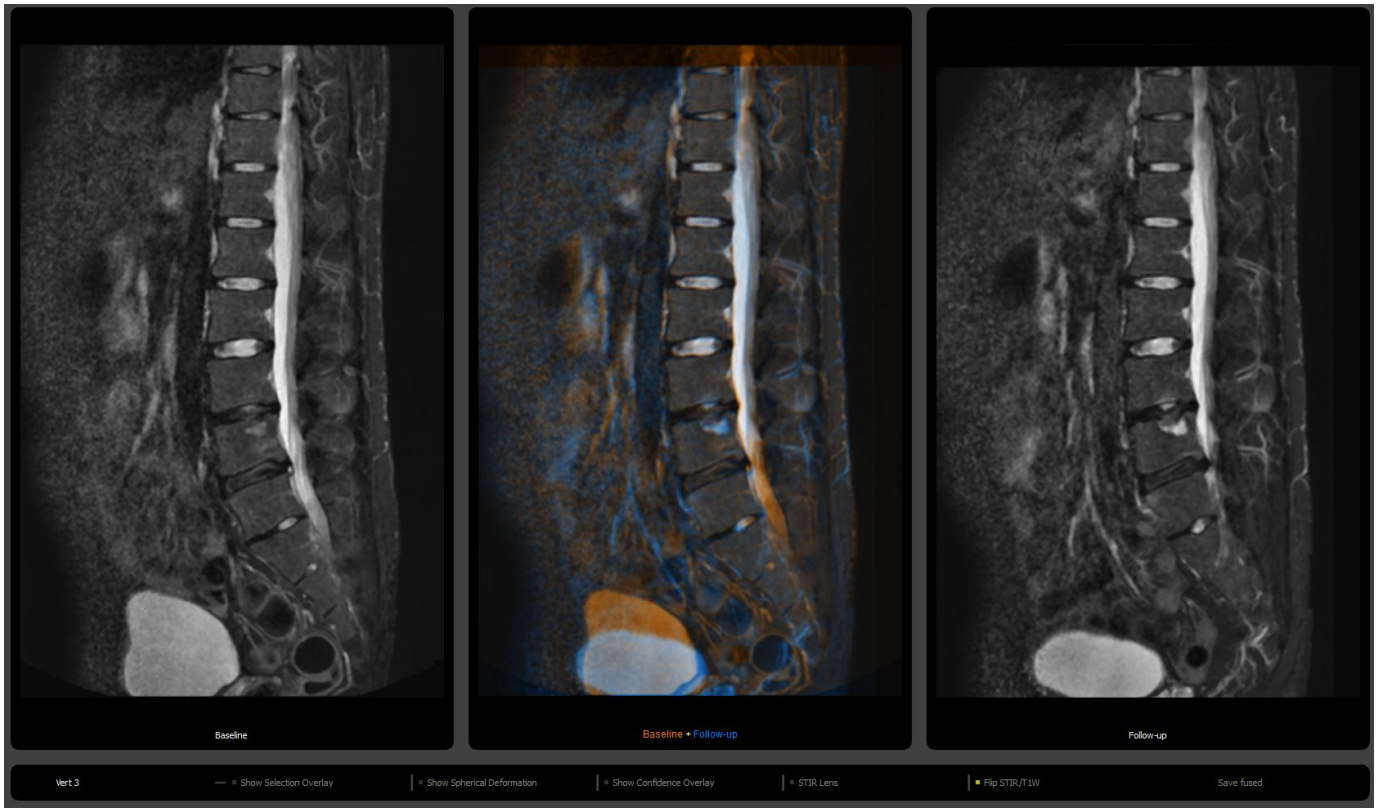

Fig. 16. Comparative visualization software.

The segmentation masks of each vertebral body are readily obtained by filling a 3D region vertically bounded by $y_{q,top}, y_{q,bot}$ and horizontally bounded by $x_{q,left}, x_{q,right}(z)$. The coordinates of segmented voxels are then transferred back from CPR space to the original image space. An example of the resulting segmentation is shown in Fig. 15.

III. Comparative Visualization of Inflammatory Lesions

A. *Locally Rigid Registration*

In this section, we employ the obtained vertebral body segmentations for locally rigid registration of baseline and

(a)

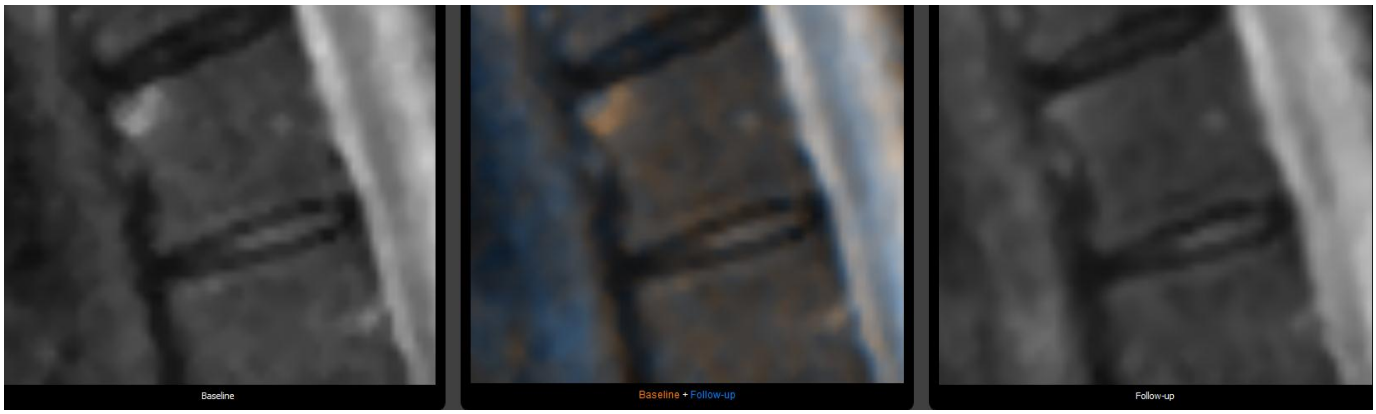

(b)

Fig. 17. Comparative assessment of axial SpA inflammatory lesions. (a) Segmentation mask (white) used for locally rigid transform estimation overlaid on the vertebral body of interest. (b) Decrease in STIR intensity in vertebra's corner (corresponding to decrease in inflammation) between baseline and follow-up highlighted with orange color in the color-fused view.

follow-up MRI of the spine in axial SpA patients. We apply the method by Dzyubachyk *et al.* [30] in which a locally rigid transform is derived from a pre-computed deformable registration. The motivation for locally rigid registration is to ensure that rigid anatomical structures, such as bones, are not deformed during baseline to follow-up registration. For example, a vertebral body, can only shift and rotate between two scans, but not stretch.

The deformable registration is computed over the entire baseline and follow-up volumes (after correcting for intensity inhomogeneity using [28]) with the `elastix` [31] software package. The method uses a multi-resolution elastic registration algorithm in which a deformable B-spline grid is incrementally refined with Mattes mutual information [32] as the similarity metric. Then, a segmentation of the rigid structure of interest, the vertebral body, in the baseline volume is used as a set of landmark voxels to estimate the rigid part of the global transformation via the landmark transform [33]. Note that it is not necessary to segment the entire vertebral body, as long as significant portion of the voxels are correctly segmented. In fact, it is preferable to under-segment the vertebra, rather than over-segment, since leakages into non-rigid structures will have a more adverse effect on the rigid transform approximation.

The described locally rigid registration method was implemented in [30] using C++, the Insight Toolkit [34], and OpenGL API. In this work, we adopted the code to use the segmentations obtained from the method of Section II as the input landmark voxels for locally rigid transform estimation. A screenshot of the comparative visualization software is shown in Fig. 16. It provides a synchronized, co-registered view of the baseline and follow-up volumes with the option of switching between T1-weighted and STIR sequences using a single mouse-click. A key feature of this software is the color-fused view (middle of Fig. 16), which displays the color-coded difference between follow-up and baseline images after the locally rigid transform has been applied. Orange color represents areas where intensity has decreased in the follow-up image compared to the baseline, while blue color represents areas where intensity has increased in the follow-up image compared to the baseline. The advantage of using such a color-encoded difference view is that the user searching for structural difference over time can focus her/his attention on a single image, rather than two images as done currently in clinical practice. Since the locally rigid transform must be computed separately for each vertebral body, the user has the

option to select the vertebra of interest from a scrolling list. The software will then apply the pre-computed segmentation mask [Fig. 17(a)] to estimate the locally rigid transform. Fig. 17(b) illustrates how a typical time change in axial SpA lesion can be efficiently visualized using the software.

B. Experiments and Results

We evaluated the proposed approach to computer-aided assessment of time changes in inflammatory lesions of axial SpA patients on a group of 3 patients from the SPondyloArthritis Caught Early (SPACE) cohort [35] at Leiden University Medical Center (LUMC) in Leiden, the Netherlands. For each patient, two random time points were selected for evaluation. The "baseline" and "follow-up" labels were also assigned randomly, so the expert reader would not have prior knowledge of the time order.

An expert reader was asked to use the comparative visualization software to evaluate the occurrence/remission of inflammatory lesions between baseline and follow-up MRI scans. The reader examined the quadrants of each of the 23 vertebral units (VUs), defined as the region including adjacent vertebral endplates [5] [Fig. 18], using the color-fused view as an indicator for locations of potential change in inflammation. For those locations which the reader considered to represent potential inflammatory change, the baseline and follow-up views were used for additional evaluation. If the reader's final assessment was "increase" in inflammation a score of +1 was given to the corresponding VU quadrant. Similarly, if the reader's final assessment was "decrease" in inflammation a score of -1 was given to the corresponding VU quadrant. If no change was detected, a score of 0 was assigned.

For ground truth comparison, we used SPARCC [7] scores assigned to each of the time points by another expert reader. The SPARCC method is designed for evaluating the presence of inflammatory lesions, rather than change in time. Therefore,

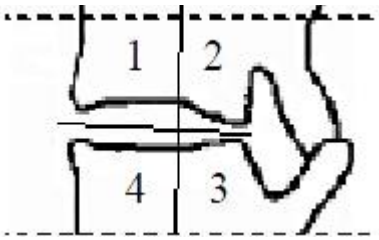

Fig. 18. Vertebral unit definition [5].

we restricted our analysis to those VU quadrants where a full appearance/remission of a lesion occurred, according to the SPARCC scores. In particular, for each VU, we summed the SPARCC scores across the slices, obtaining a total score for each of the four quadrants. If at baseline the quadrant's total SPARCC score was 0, but at follow-up it increased, it was included in the analysis. Likewise, if at baseline a quadrant's total SPARCC score was non-zero, but at follow-up became 0, it was included in the analysis. For comparison with results of our experiment, these two cases were assigned a score of +1 and -1, respectively.

We evaluated the precision and recall of our scores with respect to the SPARCC scores, separately for increase and decrease in inflammation. The results are shown in Table I.

TABLE I
PRECISION VS. RECALL FOR DECREASE AND INCREASE IN INFLAMMATION

	Precision	Recall
Decrease in inflammation	100%,	87.5%
Increase in inflammation	100%	71.4%

These results validate that the proposed semi-automated method for comparative assessment of inflammatory lesions in axial SpA patients is in good agreement with the SPARCC scoring system used in clinical studies.

C. Future Work

The expert reader involved in our study confirmed the expectation that using a single color-fused view of baseline and follow-up time points for navigation saves time and simplifies the search for inflammatory changes. However, future research should measure precisely the time advantage of using the proposed comparative assessment method vs. traditional comparative scoring.

The proposed vertebral body localization scheme does not include automatic labeling of vertebral bodies. Including this feature would further simplify the use of the comparative visualization software, since currently the user has to visually validate which vertebra is covered by a specific segmentation mask.

The proposed vertebral body segmentation algorithm is of conservative nature, meaning that it tends to under-segment. As discussed earlier this does not necessarily have an adverse effect on locally rigid transform estimation, but it does limit our ability to extend this work to the problem of automatic lesion detection. Since axial SpA lesions typically appear in vertebra's corners, accurate segmentation of vertebral body's boundaries is essential to localize the quadrants of each VU. Future work should evaluate the performance of a range (learning-based, graph-cut, statistical shape modeling) of vertebrae segmentation algorithms on MRI images of the spine in axial SpA patients.

IV. CONCLUSION

In this work, we presented a semi-automated framework for comparative visualization of inflammatory lesions in MRI of the spine in axial SpA patients. To our knowledge, this is the first attempt to perform computer-aided comparative assessment of axial SpA inflammatory lesions. We proposed a fully automated algorithm for localization and segmentation of vertebral bodies based on the quasi-periodicity of vertebral column intensity profile and tissue class probability maps. The obtained segmentations were used to derive a locally rigid registration between baseline and follow-up scans of 3 axial SpA patients. For each locally-registered vertebral unit, an

expert reader used a color-encoded difference view to evaluate increase/decrease in inflammation between baseline and follow-up scans. Results showed good agreement with SPARCC scores for cases of full lesion occurrence/remission, with 100% precision in both decrease and increase in inflammation, and 87.5% and 71.4% recall for decrease and increase in inflammation, respectively. These results indicate that the presented computer-aided comparative visualization approach has large potential in supporting clinicians in detection of inflammatory changes in MRI of the spine in axial SpA patients.

REFERENCES

[1] M. Rudwaleit, H. Haibel, X. Baraliakos, J. Listing, E. Märker-Hermann, H. Zeidler, J. Braun, and J. Sieper, "The early disease stage in axial spondylarthritis: results from the German Spondyloarthritis Inception Cohort," *Arthritis Rheum.*, vol. 60, no. 3, pp. 717–727, Mar. 2009.

[2] K. Granfors, E. Märker-Hermann, F. de Keyser, M. A. Khan, E. M. Veys, and D. T. Y. Yu, "The cutting edge of spondylarthropathy research in the millennium.," *Arthritis Rheum.*, vol. 46, no. 3, pp. 606–613, Mar. 2002.

[3] R. Carmona, S. Harish, D. D. Linda, G. Ioannidis, M. Matsos, and N. A. Khalidi, "MR imaging of the spine and sacroiliac joints for spondyloarthritis: influence on clinical diagnostic confidence and patient management.," *Radiology*, vol. 269, no. 1, pp. 208–215, Oct. 2013.

[4] W. P. Maksymowych, "Imaging in spondyloarthritis," in *Molecular Mechanisms of Spondyloarthropathies SE - 2*, vol. 649, C. López-Larrea and R. Díaz-Peña, Eds. Springer New York, 2009, pp. 17–36.

[5] J. Braun, X. Baraliakos, W. Golder, J. Brandt, M. Rudwaleit, J. Listing, M. Bollow, J. Sieper, and D. van der Heijde, "Magnetic resonance imaging examinations of the spine in patients with ankylosing spondylitis, before and after successful therapy with infliximab: evaluation of a new scoring system," *Arthritis Rheum.*, vol. 48, no. 4, pp. 1126–1136, Apr. 2003.

[6] M. Rudwaleit, S. Schwarzlose, J. Listing, J. Brandt, J. Braun, and J. Sieper, "Is there a place for magnetic resonance imaging (MRI) in predicting a major clinical response (BASDAI 50%) to TNF alpha blockers in ankylosing spondylitis?," *Arthritis Rheum.*, vol. 50, no. S211, 2004.

[7] W. P. Maksymowych, R. D. Inman, D. Salonen, S. S. Dhillon, R. Krishnananthan, M. Stone, B. Conner-Spady, J. Palsat, and R. G. W. Lambert, "Spondyloarthritis Research Consortium of Canada magnetic resonance imaging index for assessment of spinal inflammation in ankylosing spondylitis," *Arthritis Rheum.*, vol. 53, no. 4, pp. 502–509, Aug. 2005.

[8] R. G. W. Lambert, S. J. Pedersen, W. P. Maksymowych, P. Chiowchanwisawakit, and M. Østergaard, "Active inflammatory lesions detected by magnetic resonance imaging in the spine of patients with spondyloarthritis - definitions, assessment system, and reference image set," *J. Rheumatol. Suppl.*, vol. 84, pp. 3–17, Dec. 2009.

[9] D. Major, J. Hladůvka, F. Schulze, and K. Bühler, "Automated landmarking and labeling of fully and partially scanned spinal columns in CT images," *Med. Image Anal.*, vol. 17, no. 8, pp. 1151–1163, Dec. 2013.

[10] Zhuowen Tu, "Probabilistic boosting-tree: learning discriminative models for classification, recognition, and clustering," in *Tenth IEEE International Conference on Computer Vision (ICCV'05) Volume 1*, 2005, vol. 2, pp. 1589–1596 Vol. 2.

[11] S. Kadoury, H. Labelle, and N. Paragios, "Spine segmentation in medical images using manifold embeddings and higher-order MRFs," *IEEE Trans. Med. Imaging*, vol. 32, no. 7, pp. 1227–1238, Jul. 2013.

[12] A. Rasoulian, R. Rohling, and P. Abolmaesumi, "Lumbar spine segmentation using a statistical multi-vertebrae anatomical shape+pose model," *IEEE Trans. Med. Imaging*, vol. 32, no. 10, pp. 1890–1900, Oct. 2013.

[13] A. Rasoulian, R. Rohling, and P. Abolmaesumi, "Group-wise registration of point sets for statistical shape models," *IEEE Trans. Med. Imaging*, vol. 31, no. 11, pp. 2025–2034, Nov. 2012.

[14] S. Tan, J. Yao, M. M. Ward, L. Yao, and R. M. Summers, "Computer aided evaluation of ankylosing spondylitis using high-resolution CT," *IEEE Trans. Med. Imaging*, vol. 27, no. 9, pp. 1252–1267, Sep. 2008.

[15] D. Štern, B. Likar, F. Pernuš, and T. Vrtovec, "Automated detection of spinal centrelines, vertebral bodies and intervertebral discs in CT and MR images of lumbar spine," *Phys. Med. Biol.*, vol. 55, no. 1, pp. 247–264, Jan. 2010.

[16] D. Štern, B. Likar, F. Pernuš, and T. Vrtovec, "Parametric modelling and segmentation of vertebral bodies in 3D CT and MR spine images," *Phys. Med. Biol.*, vol. 56, no. 23, pp. 7505–7522, Dec. 2011.

[17] A. K. Jerebko, G. P. Schmidt, X. Zhou, J. Bi, V. Anand, J. Liu, S. Schoenberg, I. Schmuecking, B. Kiefer, and A. Krishnan, "Robust parametric modeling approach based on domain knowledge for computer aided detection of vertebrae column metastases in MRI," *Inf. Process. Med. Imaging*, vol. 20, pp. 713–724, Jan. 2007.

[18] Z. Peng, J. Zhong, W. Wee, and J.-H. Lee, "Automated vertebra detection and segmentation from the whole spine MR images," *Conf. Proc. IEEE Eng. Med. Biol. Soc.*, vol. 3, pp. 2527–2530, Jan. 2005.

[19] S. K. Michopoulou, L. Costaridou, E. Panagiotopoulos, R. Speller, G. Panayiotakis, and A. Todd-Pokropek, "Atlas-based segmentation of degenerated lumbar intervertebral discs from MR images of the spine," *IEEE Trans. Biomed. Eng.*, vol. 56, no. 9, pp. 2225–2231, Sep. 2009.

[20] D. Pham, "Spatial models for fuzzy clustering," *Comput. Vis. Image Underst.*, vol. 84, no. 2, pp. 285–297, Nov. 2001.

[21] R. Shi, D. Sun, Z. Qiu, and K. L. Weiss, "An efficient method for segmentation of MRI spine images," *2007 IEEE/ICME Int. Conf. Complex Med. Eng.*, pp. 713–717, May 2007.

[22] J. Carballido-Gamio, S. J. Belongie, and S. Majumdar, "Normalized cuts in 3-D for spinal MRI segmentation," *IEEE Trans. Med. Imaging*, vol. 23, no. 1, pp. 36–44, Jan. 2004.

[23] C. Fowlkes, S. Belongie, and J. Malik, "Efficient spatiotemporal grouping using the Nystrom method," in *Proceedings of the 2001 IEEE Computer Society Conference on Computer Vision and Pattern Recognition. CVPR 2001*, 2001, vol. 1, pp. I–231–I–238.

[24] J. Egger, T. Kapur, T. Dukatz, M. Kolodziej, D. Zukić, B. Freisleben, and C. Nimsky, "Square-cut: a segmentation algorithm on the basis of a rectangle shape," *PLoS One*, vol. 7, no. 2, p. e31064, Jan. 2012.

[25] S.-H. Huang, Y.-H. Chu, S.-H. Lai, and C. L. Novak, "Learning-based vertebra detection and iterative normalized-cut segmentation for spinal MRI," *IEEE Trans. Med. Imaging*, vol. 28, no. 10, pp. 1595–1605, Oct. 2009.

[26] S.-H. Huang, Q.-J. Wu, and S.-H. Lai, "Improved AdaBoost-based image retrieval with relevance feedback via paired feature learning," *Multimed. Syst.*, vol. 12, no. 1, pp. 14–26, Apr. 2006.

[27] M. A. Fischler and R. C. Bolles, "Random sample consensus: a paradigm for model fitting with applications to image analysis and automated cartography," *Commun. ACM*, vol. 24, no. 6, pp. 381–395, Jun. 1981.

[28] O. Dzyubachyk, R. J. van der Geest, M. Staring, P. Börnert, M. Reijnierse, J. L. Bloeml, and B. P. F. Lelieveldt, "Joint intensity inhomogeneity correction for whole-body MR data," *Med. Image Comput. Comput. Assist. Interv.*, vol. 16, no. Pt 1, pp. 106–13, Jan. 2013.

[29] A. Kanitsar, D. Fleischmann, R. Wegenkittl, P. Felkel, and E. Groller, "CPR - curved planar reformation," in *IEEE Visualization, 2002. VIS 2002.*, 2002, pp. 37–44.

[30] O. Dzyubachyk, J. Blaas, C. P. Botha, M. Staring, M. Reijnierse, J. L. Bloem, R. J. van der Geest, and B. P. F. Lelieveldt, "Comparative exploration of whole-body MR through locally rigid transforms," *Int. J. Comput. Assist. Radiol. Surg.*, vol. 8, no. 4, pp. 635–647, Jul. 2013.

[31] S. Klein, M. Staring, K. Murphy, M. A. Viergever, and J. P. W. Pluim, "elastix: a toolbox for intensity-based medical image registration," *IEEE Trans. Med. Imaging*, vol. 29, no. 1, pp. 196–205, Jan. 2010.

[32] D. Mattes, D. R. Haynor, H. Vesselle, T. K. Lewellen, and W. Eubank, "PET-CT image registration in the chest using free-form deformations," *IEEE Trans. Med. Imaging*, vol. 22, no. 1, pp. 120–128, 2003.

[33] B. K. P. Horn, "Closed-form solution of absolute orientation using unit quaternions," *Journal of the Optical Society of America A*, vol. 4, no. 4. pp. 629–642, 1987.

[34] L. Ibanez, W. Schroeder, L. Ng, and J. Cates, "The ITK Software Guide," *The ITK Software Guide*, 2005. [Online]. Available: http://www.itk.org/ItkSoftwareGuide.pdf.

[35] R. van den Berg, M. de Hooge, F. van Gaalen, M. Reijnierse, T. Huizinga, and D. van der Heijde, "Percentage of patients with

spondyloarthritis in patients referred because of chronic back pain and performance of classification criteria: experience from the Spondyloarthritis Caught Early (SPACE) cohort," *Rheumatology (Oxford)*, vol. 52, no. 8, pp. 1492–1499, Aug. 2013.